water

MDPI

Article

Numerical Analysis of Wind Effect on Wave Overtopping on a Vertical Seawall

Angela Di Leo [1], Fabio Dentale [1], Mariano Buccino [2], Sara Tuozzo [2,*] and Eugenio Pugliese Carratelli [1]

[1] Department of Civil Engineering, University of Salerno, Via Giovanni Paolo II, 132, 84084 Fisciano, Italy
[2] Department of Civil, Architectural and Environmental Engineering, University of Napoli "Federico II", Via Claudio 21, 80125 Napoli, Italy
* Correspondence: sara.tuozzo@unina.it

Abstract: Onshore wind significantly affects wave run-up and overtopping, thereby representing a major variable to account for in the design process. The aim of this study is to analyze the ability of numerical models to properly reproduce the wind effect on the overtopping at vertical seawall and to use them to understand how the wind influences the overtopping process as well. We use the RANS model, FLOW-3D, and the NLSW model, SWASH; both model the action of wind through the shear stress that it exerts on the sea surface. Although a simplified modelling of wind has been adopted, the CFD model has led to physically consistent results. On the other hand, SWASH seems to be unsuitable for reproducing the enhancement of the overtopping rate due to wind. CFD numerical results show that the wind affects only the lower overtopping regime (i.e., $q < 1$ l/s/m); as the mean overtopping discharge decreases, the influence of wind increases. Specifically, wind plays a key role in pure "white overtopping", where the advection of spray is the predominant mechanism of the overtopping process. The effects of wind thus seem to be important in the design of seawalls, but are difficult to quantify through hydraulic models because of the unknown scaling laws. Therefore, we have found that a full-scale numerical approach is suitable to study the influence of wind on wave overtopping and to evaluate the wind factor to take into account in the design process.

Keywords: wind stress; wave overtopping; computational fluid dynamics; SWASH

Citation: Di Leo, A.; Dentale, F.; Buccino, M.; Tuozzo, S.; Pugliese Carratelli, E. Numerical Analysis of Wind Effect on Wave Overtopping on a Vertical Seawall. *Water* **2022**, *14*, 3891. https://doi.org/10.3390/w14233891

Academic Editors: Felice D'Alessandro and Chin H Wu

Received: 18 October 2022
Accepted: 25 November 2022
Published: 29 November 2022

1. Introduction

The onshore wind that blows during storms can significantly enhance wave run-up and overtopping. It is therefore an important variable to account for in the design of coastal defenses against flooding.

As previously described [1], the existing guidelines on wave overtopping need to be extended to take into account several factors in predicting wave overtopping discharges (e.g., the presence of oblique sea and swell conditions). Among these factors, much re-search has demonstrated the importance of wind effect on the wave overtopping phenomenon.

In particular, the smaller the mean overtopping discharge, the greater its growth rate due to the presence of wind. Therefore, the wind has a different influence on the "green overtopping" (when the wave overtopping runs over the crest of the structure in a coherent water mass) and the "white overtopping" (a non-continuous overtopping and/or a significant volume of spray) [2]. As previously reported [2], a mean overtopping discharge below 1 l/s/m might increase up to four times under strong winds. Since this order of magnitude represents the threshold for structural damages and pedestrians and vehicles safety (which can be endangered by the presence of water spray due to the wind that may reduce visibility on highways and roads) [2], a significant growth in the mean overtopping discharge due to the wind needs to be considered in the design process.

However, despite previous research and field observations indicating that wind can influence the overtopping rate, the comprehension and estimation of its effect are still characterized by uncertainties.

This lack of sufficient knowledge is due to shortcomings of the investigation model and difficulties associated with field measurements. Physical models experience complications in studying a phenomenon that requires two different scale laws (i.e., Froude and Reynolds), while field measurements are limited to the local wave and wind conditions. However, the effect of wind on overtopping has mainly been investigated through physical model studies or field experiments [3–6], whereas there have been few numerical investigations [7–9]. Nevertheless, numerical analysis has the advantage of avoiding scale effects associated with physical model experiments and of extending wave, wind and geometric characteristics investigated as compared to field tests.

Recently, with the large variety of factors that can affect the overtopping process, the use of algorithms such as the Compressive Sensing (CS) technique is finding increased favor in several coastal engineering applications [10–12]. The algorithm CS ensures the development of cheaper and faster overtopping and run-up estimation systems, characterized by lower cost and data storage requirements as compared to the existing tools.

In this study, we use two numerical models to assess the role of wind on the mean overtopping discharge at a vertical seawall. One model, more accurate, is based on the Reynolds Averaged Navier-Stokes equations and the other, a simplified (i.e., depth-integrated) model, is based on the Non-Linear Shallow Water equations; both of which take wind into account through the shear stress it exerts on the sea surface.

Specifically, the CFD multi-physics solver FLOW-3D HYDRO [13] and SWASH [14] have been employed.

Although we have employed the single-phase approach in this study, it is worth noting that FLOW-3D can adopt either a single or a multi-phase approach to reproduce the presence of the wind. Despite the latter approach representing a more rigorous numerical modelling, we aim to demonstrate that this simplified modelling suffices to represent the process in its macro properties (i.e., the influence of the wind on the mean overtopping discharge).

RANS models are widely employed to study wave-structure interaction problems, such as wave run-up and overtopping [15–20]. Furthermore, they have also been used to investigate the effects of wind on the overtopping process [8,21,22]. On the other hand, SWASH has been used to estimate wave overtopping [23,24], but, to the authors' knowledge, it has never been used to study the influence of wind.

The aim of this study is twofold:

- to verify the ability of these numerical models to correctly reproduce the influence of wind on the overtopping rate, even though simplified wind modelling has been used;
- to clarify how the wind acts and how its effect on the enhancement of the overtopping rate changes depending on the overtopping regime.

The paper is organized as follows. First, the state of the art of the main studies conducted so far and the models used is explained. Next, the numerical models employed in this study are described, as well as the numerical setup and the study campaign. The central part of the work then deals with the numerical results and their comparison with the findings from the literature. Finally, accomplishments, short-comings and starting points for future research are discussed.

2. Literature

It has long been known that onshore winds significantly increase wave run-up and overtopping during storms [3,25].

The impact on the overtopping process has been studied mainly through physical model experiments so far, although some numerical research has been published in recent times.

Among the physical model studies, ref. [3] used a paddle wheel to "push ahead" the water reaching the crest of a vertical wall. The authors observed that part of the breaker spray, which would have fallen back into the sea without wind, was blown, instead, over the structure. It was found out that this process can increase the mean overtopping discharge ($q_{NO\text{-}WIND}$) by a factor of 3.2.

The same experimental approach was employed by [26] for sloping structures; compared to vertical walls, a greater enhancement factor was found, reaching a value of 6.2. By setting up four fans in front of an upright structure, [3,5] argued that the wind only affects lower overtopping regime, namely $q_{NO\text{-}WIND} < 10^{-2}$ m^3/s/m, approximately. Furthermore, by gathering field and laboratory data the following formula was proposed, which relates the wind transport factor f_{WIND} to the overtopping regime:

$$f_{WIND} = \frac{q_{WIND}}{q_{NO-WIND}} = 1 + 3\left(\frac{-\log q_{NO-WIND} - 2}{3}\right)^3 \quad 10^{-5} < q_{NO-WIND} < 10^{-2} \quad (1)$$

According to [4], f_{WIND} ranges between 1 (negligible effect of wind) and 4.

Remarkably, the authors find a reasonable consistency between field and laboratory data, although the latter may experience challenges with regard to scaling droplets and the turbulent spray phenomenon. In fact, this finding seems to suggest that the high velocities attained during the overtopping events make the process highly turbulent, and independent of the Reynolds number.

In [6], the presence of wind was simulated by positioning an exhaust fan at the beginning of the flume. Results indicate that the overtopping rate increases with growing wind speed, and that the influence of wind is greater with shorter waves. These findings were subsequently corroborated by experiments conducted by Durbridge at the University of Plymouth [27]. Examining the response of a shallow water vertical seawall under both regular and irregular waves, the author showed that high wind transport factors could occur even for an overtopping regime as high as 10 l/s/m.

As already mentioned, the numerical investigations were carried out more recently. The authors of [7] used the single-phase numerical model CADMAS-SURF to analyze the response of both vertical and sloping walls, stressing out a positive correlation between wind speed and overtopping enhancement factors. Analogous to our study, CADMAS-SURF accounts for the presence of wind via the shear stress it exerts on the water surface.

Similar outcomes were presented in [21] based on a two fluid Navier Stokes model, which also showed that the wind field may significantly affect the wave profile. The authors found a maximum wind factor of 1.25. Consistently, the CFD study by [9] found values of f_{WIND} between 1.3 and 1.5.

A two-fluids approach has been also implemented by [9] to study the wind effects on a breaking solitary wave. It was observed that wind alters the air flow structure above the water, increases the generation of vorticity and turbulent stress, and affects the wave shoaling, breaking and run-up processes.

3. Numerical Models

In this section, the RANS and NLSW models are briefly explained.

3.1. FLOW-3D

FLOW-3D solves the Reynolds-Averaged Navier–Stokes (RANS) equations using a Eulerian approach under the assumption of incompressible fluid flow. Imposing continuity within the flow, the following system is then solved:

$$\frac{\partial u_i}{\partial x_i} = 0 \quad (2)$$

$$\frac{\partial u_i}{\partial t} + u_j \frac{\partial u_i}{\partial x_j} = -\frac{1}{\rho}\frac{\partial p}{\partial x_i} + \frac{\partial}{\partial x_j}\left[(\nu + \nu_T)\left(\frac{\partial u_i}{\partial x_j} + \frac{\partial u_j}{\partial x_i}\right)\right] + g_i = 0 \quad (3)$$

where u is the time averaged velocity, ρ is the fluid density, p is the pressure, ν is the kinematic viscosity, ν_t is the eddy viscosity and g is the gravity acceleration. Turbulence in the flow is accounted for with the RNG k-ε model [28].

The eddy viscosity ν_t in RANS equations is determined through the RNG *k*-ε model, with the equations for the turbulent kinetic energy k and the specific turbulent dissipation ε, as follows:

$$\frac{\partial k}{\partial t} + u_j \frac{\partial k}{\partial x_j} - \frac{\partial}{dx_j}\left[\frac{(\nu + \nu_T)}{\sigma_k}\frac{\partial k}{\partial x_j}\right] + \varepsilon - P = 0 \quad (4)$$

$$\frac{\partial \varepsilon}{\partial t} + u_j \frac{\partial \varepsilon}{\partial x_j} - \frac{\partial}{dx}\left[\frac{(\nu + \nu_T)}{\sigma_\varepsilon}\frac{\partial \varepsilon}{\partial x_j}\right] + c_2\frac{\varepsilon^2}{k} - c_1\frac{\varepsilon}{k}\nu_T P + R = 0 \quad (5)$$

The Equations (2)–(5) have been finite-difference solved; the flow region is subdivided into a mesh of fixed rectangular cells, at the center of which are located all the variables but velocities, which are situated instead at the cell–faces (staggered grid arrangement). The free surface is tracked according to the Volume of Fluid (VOF) technique [29]. Curved obstacles, wall boundaries, or other geometric features are embedded in the mesh by defining the fractional areas of the cells that are open to flow (FAVOR™ method) [30].

FLOW-3D uses variable time stepping to maintain the stability and accuracy of the solution. In particular, the n-th time step size Δt^n is automatically adjusted to:

$$\Delta t^n = \min(\Delta t^n_{CON},\ \Delta t_s) \quad (6)$$

where Δt_s is a user defined sampling rate which depends on the frequency spectrum of the phenomenon under study, and Δt^n_{CON} is a convergence time step size that is needed to avoid numerical instabilities. Since the advective fluxes have been computed using a simple first order donor cell, $\Delta t^n_{CON} t$ is required to meet the following criterion:

$$\Delta t^n_{CON} = \min(0.5 \cdot \Delta t_{CFL},\ 0.5\frac{\Delta x}{\sqrt{\Delta z \Delta a_z}}) \quad (7)$$

where Δt_{CFL} is the time step to satisfy the Courant–Friedrichs–Lewy (CFL) stability criterion, and the second quantity at the right-hand side of Equation (7) ensures surface waves cannot propagate more than one cell in one time step (a_z indicates vertical acceleration).

The CFD Wind Stress Model

The approach followed here is different from the previous work described above: the influence of the wind is assumed to depend upon the surface stress acting on the water surface in the stretch of water closer to the shore.

A two-dimensional numerical model has therefore been implemented at field scale through a simple wind model, to evaluate the stress induced by the wind on the sea surface.

If the vertical distribution of the sea wind follows logarithmic law, the wind shear stress acting on the sea surface is typically estimated by Equation (8). It utilizes the wind speed U_{10} at an elevation of 10 m above sea level, and the sea surface drag coefficient C_{D10}, and reads:

$$\vec{\tau_s} = \rho_a C_{D10} |\vec{U_{10}}| U_{10} \quad (8)$$

where:

ρ_a is the density of air (1.225 kg m^{-3}),

U_{10} is the wind velocity at 10 m above the water surface,

C_{D10} is the wind shear coefficient (or drag coefficient).

The wind stress model can be applied in FLOW-3D defining wind velocity (U_{10}) and wind shear parameters (ρ_a; C_{D10}).

3.2. SWASH

SWASH is an open-source time domain wave model [14], that integrates the non-linear shallow water equations with a non-hydrostatic pressure term:

$$\frac{\partial \zeta}{\partial t} + \frac{\partial hu}{\partial x} = 0 \quad (9)$$

$$\frac{\partial u}{\partial t} + u\frac{\partial u}{\partial x} + g\frac{\partial \zeta}{\partial x} + \frac{1}{2}\frac{\partial p_b}{\partial x} + \frac{1}{2}\frac{p_b}{h}\frac{\partial(\zeta - d)}{\partial x} + c_f\frac{u|u|}{h} = 0 \quad (10)$$

$$\frac{\partial \omega_s}{\partial t} = \frac{2p_b}{h} - \frac{\partial \omega_b}{\partial t},\ \omega_b = -u\frac{\partial d}{\partial x} \quad (11)$$

$$\frac{\partial u}{\partial x} + \frac{\omega_s - \omega_b}{h} = 0 \quad (12)$$

where u is the depth-averaged velocity in x-direction, w_s and w_b are the velocity in z-direction at the free surface and at the bottom respectively, ζ is the free-surface elevation from the still water level, d is the still water depth and h the total depth, p_b is the non-hydrostatic pressure at the bottom, g is the gravitational acceleration and c_f is the dimensionless bottom friction coefficient.

The governing equations are based on the incompressible Navier-Stokes equations when multiple layers in the vertical are considered; therefore, SWASH can take the vertical structure of the horizontal flow into account. The wave breaking is properly modelled by means of the hydrostatic front approximation, HFA [31].

The numerical scheme adopted to solve the governing equations is an explicit, second order accurate (in space and time) finite difference method that conserves both mass and momentum at the numerical level. To satisfy Courant–Friedrichs–Lewy (CFL) condition, SWASH adopts an adaptive time step.

A detailed description of the numerical model is given in [14,31].

The SWASH Wind Stress Model

SWASH models the wind effect through the wind stress that transfers the momentum flux from wind to surface waves.

The wind stress depends on the drag coefficient and wind velocity relative to the wave celerity; it is expressed as:

$$\vec{\tau_s} = \rho_a C_D |\vec{U_{10}} - c|(U_{10} - c) \quad (13)$$

As concerns the drag coefficient, seven different formulations are available in SWASH (among them a constant value: a linear or a second order polynomial relationship between C_D and wind velocity). Major details can be found in the SWASH user manual [32]. In this study, a constant drag coefficient value was adopted.

According to [33], a heterogeneous distribution of the wind stress over a wavelength allows us to reproduce wave growth due to the wind in a phase-resolving model. The wind stress may vary with a larger wind drag on the wave crest than that in the trough. Therefore, the wind stress is applied on the wave crest only.

4. Experiments

4.1. Geometry of the Structure and Foreshore

Numerical experiments examine the enhancement of wave overtopping at a vertical seawall due to the wind. The numerical experiments were performed at prototype scale.

The geometry of the foreshore (Figure 1a) reproduced in the numerical tests derived from the previous experimental campaign on the Malecòn seawall, Habana (Cuba), conducted at University of Naples "Federico II" [34].

The foreshore rises from 18.72 m below MWL to the toe of the Malecón seawall, which is nearly at 1.70 m below MWL. In all simulations, it was considered a surge of +1.73 m, which is associated with a 50 year return period storm surge.

The foreshore is multi-slope; the bathymetry encompasses a mild stretch with a 4.1% slope, followed by a step inclined by 1:3 and an upper zone made up on two parts with a slope of 8.6% and 6%, respectively. The overall length of the slopes is 230 m. It has been preceded by a "flat area", 180 m long, which allows the waves to develop properly prior to evolving over the slopes.

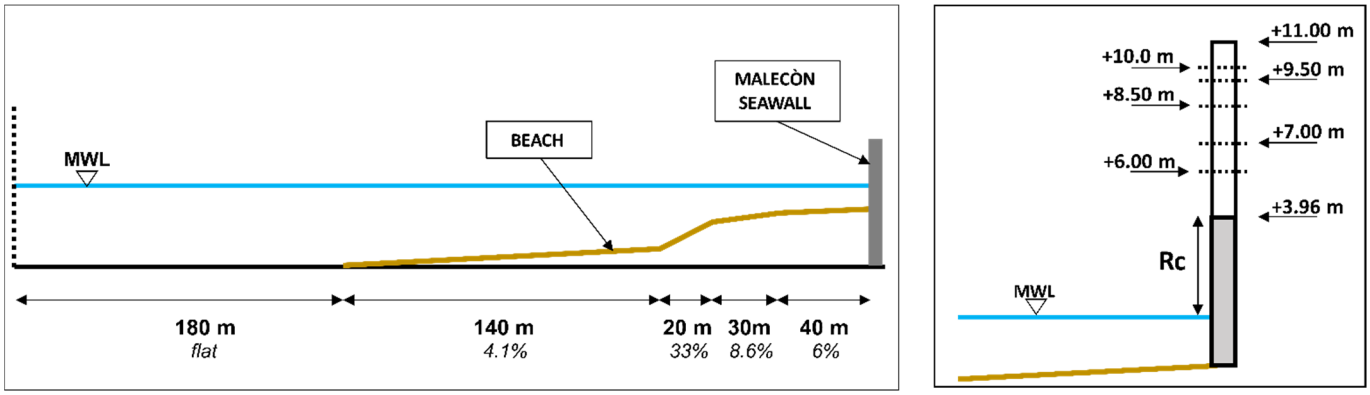

(**a**) (**b**)

Figure 1. Characteristics investigated of the Havana foreshore and Malecón seawall. Panel (**a**) sketch of bathymetry; panel (**b**) different crests freeboard of vertical wall.

At the end of the channel there is the Malecón seawall, which is a simple vertical wall with a crest freeboard, Rc, of +3.96 m above MWL.

According to the literature, the lower the mean overtopping discharge, the greater the influence of the wind. Therefore, lower discharges were analyzed by increasing Rc. Specifically, six more crest freeboards were modelled (Figure 1b).

4.2. Wind Model Implementation

The wave characteristics investigated, along with the wave celerity, are summarized in Table 1. The wave height varied from 1.5 m to 8 m, and two wave periods (10 and 12 s) were analyzed. Specifically, three breaking waves and one non-breaking wave were examined.

Table 1. Wave characteristics used for wind model implementation.

ID	H (m)	T (s)	Wave Celerity c (m/s)	
			Deep Water c_0	On 20.45 m Water Depth c
TEST_1	8	10	15.61	12.21
TEST_2	8	12	18.74	12.81
TEST_3	1.5	10	15.61	12.21
TEST_4	5.4	10	15.61	12.21

It is worth noting that not all the waves were run with the seven crest freeboards. In particular, TEST_1 was run for Rc = +10 m and Rc = +11 m, TEST_4 for Rc = +3.96 m and Rc = +11 m, whereas TEST_2 was used for Rc = +3.96 m only. TEST_3 was run with all the crest freeboards (Figure 1b), except Rc = +11 m.

A parametric study was implemented (Tables 2 and 3), using the traditional sea age ratio β, which characterizes wave conditions under the action of wind [35]:

$$\beta = \frac{c_0}{U_{10}} \tag{14}$$

Table 2. Wind model characteristics of TEST_2 (T 12 s).

U_{10}	C_{D10}	β
30	0.0025	0.62
18.7	0.0021	1.00
9.4	0.0011	1.99
6.1	0.0009	3.07
1.9	0.0010	9.86

Table 3. Wind model characteristics of TEST_1, TEST_3, TEST_4 (T 10 s).

U_{10}	C_{D10}	β
31.2	0.0026	0.50
19	0.0021	0.82
12.5	0.0015	1.25
5.2	0.0009	3.00
3.1	0.0009	5.04

According to [35], values of β between 0.5 and 1.25 may represent seas under the dominant effect of tangential wind stress; larger values, up to 10, are meant to model swells under weak winds. The drag coefficient C_{D10}, reported in Tables 2 and 3, was determined with the predictive equation suggested by [36]:

$$\sqrt{C_{D10}} = \frac{0.239 + 0.0433 \cdot \{(U_{10} - 8.271) + [0.120 \cdot (U_{10} - 8.271)^2 + 0.181]^{0.5}\}}{U_{10}} \quad (15)$$

Equation (15) is based on 7000 near surface eddy covariance flux measurements over the sea, and is consistent to other literature models, such as [37]. The formula was recently successfully employed to reconstruct the sediment pollution patterns at Bagnoli Bay, South Italy [38,39].

4.3. CFD Numerical Setup

A 2D-numerical wave flume was set up to carry out the numerical simulations.

The geometry was generated using CAD software, based on the structural characteristics described in the previous paragraph, and then imported into the code as an STL file. The computational domain (410 m in the x direction and 40 m in the z direction) had only a general mesh block, which represented the area where the fluid (the effect of air is not considered).

Numerical waves were generated at the boundary condition by using the Stokes and Cnoidal (Fourier series method, [40]) wave generator. This method possesses higher order accuracy than other wave theories [41] and it is thus recommended to generate any type of linear and nonlinear periodic waves at all water depths. The waves were determined by specifying wave period, T, wave height, H, and local still water depth, d.

The initial condition considered was a still water with no current. It is worth noticing that the still water level in the numerical simulations took into account the surge of +1.73 m described in Section 4.1 (i.e., d = 20.45 m).

In order to completely define the problem, the proper boundary conditions were applied (Figure 2).

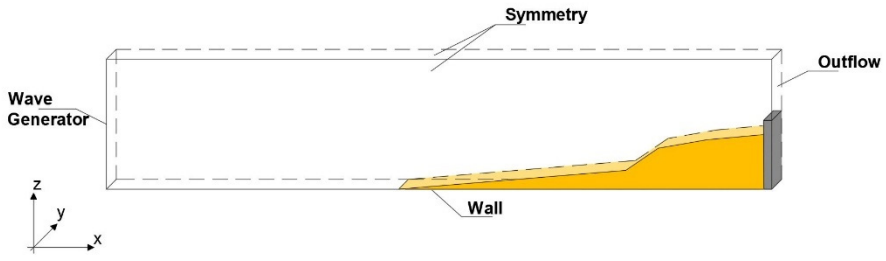

Figure 2. Boundary conditions of CFD 2D-domain.

As previously mentioned, at the left boundary a surface wave enters the computational domain and propagates in the direction normal to the boundary. At the opposite side, behind the structure, an "Outflow" condition was imposed, which lets the waves flow out the computational domain without any reflections. The lateral boundary conditions were set to "Symmetry" where the velocity gradient vanishes, and the turbulence production is zero. At the bottom, the "Wall" condition was defined, which applies a zero-velocity condition normal to the boundary.

A list of relevant numerical parameter settings of the present study is given in Table 4.

Table 4. General Parameter settings in CFD numerical simulation.

Parameter	Setting
Fluid	Water (20 °C), incompressible
Turbulence	RNG
Pressure Solver	GMRES
VOF advection	Split Lagrangian method (TruVof)
Time step control	Automatic (stability and convergence)

The computational domain was discretized in one general mesh. A grid sensitivity study was performed, and eight rectangular grids with different cell sizes were tested. Their characteristics are reported in Table 5.

Table 5. Characteristics of grids used for sensitivity analysis.

ID GRID	Δx (m)	Δz (m)
A20	2.9	1.2
A30	1.9	0.8
A40	1.5	0.6
A60	1.0	0.4
A80	0.7	0.3
A160	0.4	0.15
C278	0.25	0.30
M278	0.25	0.15

For each mesh, the volume flow rate measured on the crest of the seawall was acquired; then, the curves of cumulative overtopping volume for different grid sizes were compared (Figure 3). FLOW-3D computes the overtopping time series q(t) by extracting the volume flow rate (fluid fraction times area times velocity) at a face of the flux surface. Flux surfaces are a special subset of baffles that are used to measure quantities that flow through them.

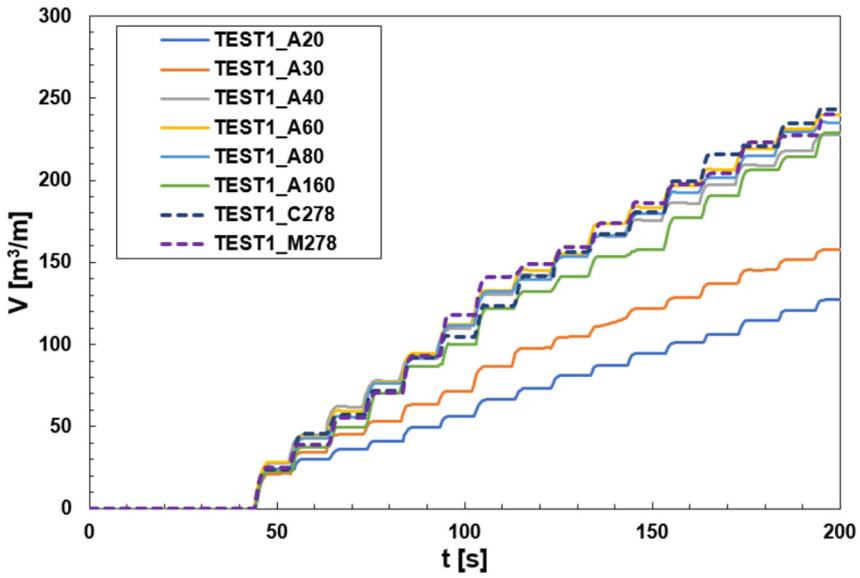

Figure 3. Cumulative overtopping volume curves for different grid sizes analysed.

A grid sensitivity study was thus carried out based on the analysis of the final overtopping volume, or similarly, the mean overtopping flow rate.

The grid effect was measured using the quantity V_E (also indicated as relative error between two consecutive grids), defined as follows:

$$V_E = \left| \frac{Vf_{finer} - Vf_{Coarser}}{Vf_{Coarser}} \right| \quad (16)$$

where $V_{f,finer}$ represents the final overtopping volume relative to the finer grid and $V_{f,coarser}$ is the analogous value for the coarser grid, which was used as reference value.

The Figure 4 shows the geometric mean of two dimensions, $\sqrt{\Delta x \Delta z}$, of the cell on the abscissa, and the absolute value of the relative error, V_E, on the ordinates. The plot indicates three main aspects: an area of increasing error as the grid decreases ($\sqrt{\Delta x \Delta z}$ between 1.8 and 1.2), a progressively decreasing phase of the error with reducing grid size ($\sqrt{\Delta x \Delta z}$ between 1.2 and 0.9), and, finally, a grid independence area ($\sqrt{\Delta x \Delta z}$ smaller than 0.9). The initial increasing trend could be interpreted as a consequence of the grid being too coarse to properly represent wave overtopping. Mesh refinement in the x direction is important for water flow even if refinement in the z direction is also important for capturing free surface position.

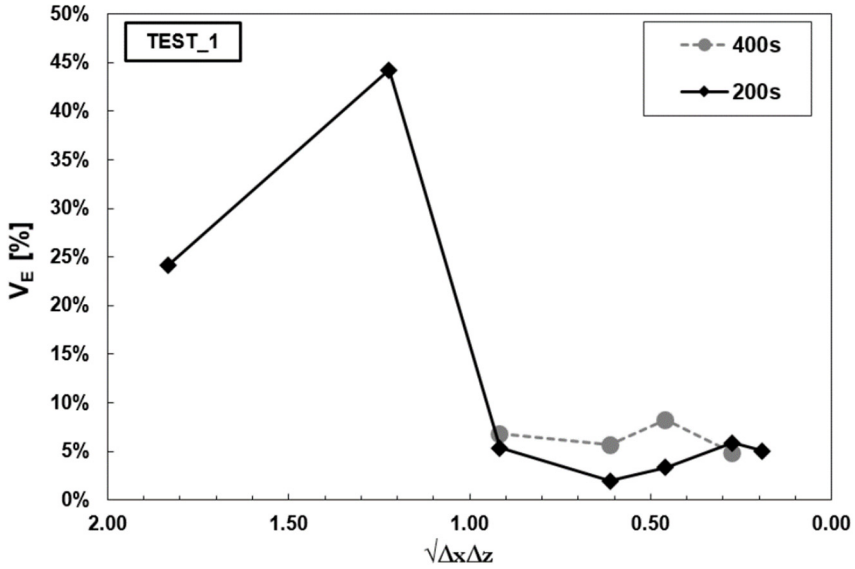

Figure 4. Relative volume error as a function of the geometric mean of two dimensions of the cell. TEST_1 (H = 8 m T = 10 s).

The grid selected was A160 (0.4 m × 0.15 m) and positioned in the grid independence area (Figure 3), where the relative volume error is lower than 10%. However, the further mesh refining in x direction (C278-M278) did not lead to significant improvement of the model result (Figure 3). The choice of this grid dimensions derived also from the compromise between accuracy of the results and computational cost, given the large extension of the numerical domain.

The final numerical layout was validated by [20] against the laboratory experiments by [34], which were carried out to investigate the overtopping response of the Malecòn under severe wave attacks dominated by breaking waves. Eight random sea-states were simulated both with and without the wall to assess the capability of the model of reproducing the overtopping process, along with the evolution of waves along the steep foreshore.

Numerical outcomes showed a good agreement with laboratory values of the mean overtopping rates; likewise, the wave spectrum at the toe of the structure was reproduced with good accuracy over the entire spectral band, including low frequency infragravity waves [42].

The latter result implies that the wave breaking process is well modelled, despite the fact that the problem of turbulence overproduction highlighted in [43,44] was not explicitly addressed.

As recently pointed out by [44], this depends on the short propagation distance prior the onset of breaking (1–2 wavelengths), which limits the turbulence overproduction problem even in the post breaking phase.

4.4. SWASH Numerical Setup

The layout shown in Figure 1a was reproduced in the numerical model at the prototype scale. Behind the Malecón seawall, a basin was modelled in order to collect water which overtopped the wall. Numerical simulations were performed in 1D-mode. At the upstream boundary, a weakly reflective boundary condition was used to avoid the reflection of waves from onshore (i.e., only entering waves were simulated). At the downstream boundary of the domain, a Sommerfeld radiation condition was applied in order to minimize the effect of reflection. A still water level was applied as the initial condition for all numerical model tests; the still water level includes the surge and thus is set to 20.45 m.

At the wave-maker, both incident time series and monochromatic waves were generated. The former was derived by the CFD tests using the method of [45] with six gauges. In particular, TEST_3 (Table 1) was performed with two crest freeboards, namely R_c = +3.96 m and +6.0 m. Numerical instabilities occurred with the other wave conditions listed in Table 1. Therefore, further tests with a monochromatic wave generation were added to investigate different magnitudes of overtopping discharge. The wave characteristics of these additional tests are listed in Table 6, where TEST_1S was performed with Rc = +6.0 m, while the other tests were performed with Rc = +3.96 m. The wind conditions examined are those listed in Table 3.

Table 6. Wave characteristics of additional tests performed with SWASH.

ID	H (m)	T (s)
TEST_1S	0.95	10
TEST_2S	0.8	10
TEST_3S	0.7	10
TEST_4S	0.6	10

The grid size used was 1 m; in vertical direction, 2 layers were employed. The Manning coefficient of n = 0 $m^{-1/3}$ s was used. The default values of breaking parameters [31] were adopted in the numerical simulations. The non-hydrostatic pressure term was applied with a Keller-box scheme. An adaptive time step was implemented to satisfy the Courant–Friedrichs–Lewy (CFL) condition, with a time step restriction set to a maximum Courant number of 0.5.

A time series of overtopping layer thickness, h(t), and the depth-averaged overtopping velocity, u(t), were extracted at the seawall crest. Their product gave the overtopping rate q(t) per unit length; then, the mean overtopping discharge was obtained by integrating q(t) over the test duration.

5. Results

5.1. Physical Processes and Basic Definitions

According to the literature [3,46], the wind shear can affect wave overtopping either by raising the mean sea level ($\overline{\eta}$) or by acting on the wave profile at the wall.

The effects on the wave profile encompass either the change in phase-averaged and time-domain wave properties (e.g., variation of the wave height and profile skewness), the deformation of the runup wedge, or the onshore drift of the droplets produced during the up-rush process.

The effect on the mean sea level includes wind and wave setups.

The amount of wind setup, $\overline{\eta_{WIND}}$, is governed by the cross-shore balance between the time-averaged wind stress, $\overline{\tau_w}$, and the hydrostatic forces [47]:

$$\rho_w g[h\,(x) + \overline{\eta_{WIND}}] \cdot \frac{d\overline{\eta_{WIND}}}{dx} - \overline{\tau_w} = 0 \tag{17}$$

which can be integrated and parametrized in terms of the quantity:

$$A = (n \cdot \overline{\tau_w} \cdot l_D)/\rho_w g\, h_0^2 \tag{18}$$

The variable A represents the shear to hydrostatic force ratio; in Equation (18), $n \cong 1.5$ accounts for the effects of bottom friction, l_D is the domain's length and h_0 denotes the offshore water depth.

The change in wave setup (or set-down), $\overline{\eta_{WAVE}}$, is related to a change in the radiation stress gradient, dS_{xx}/dx, caused by variation in the wave profile characteristics. According to [48], the gradient is seawards for non-breaking waves, while it is directed towards the shore for breaking waves.

A change in the breaking point with the wind can also produce a variation in $\overline{\eta_{WAVE}}$; as the breaking point moves offshore the wave setup increases, and vice-versa.

In this regard, it is worth mentioning that the incipient breaking condition is intended here as the wave profile that becomes nearly vertical at any point of the foreshore, with a clear departure of a plunging jet from the wave crest. This is consistent with the great majority of literature, e.g., [49–51].

In many aspects of the discussion below, non-breaking and breaking waves are analysed separately.

5.2. On the Role of the Mean Water Level

Despite the complexity of the processes that rule its variation in response to wind stress, $\overline{\eta}$ plays a subordinate role globally in this study.

First, we note that the length of the computational domain (l_D = 410 m) is too small for a significant wind setup to occur. Using the maximum wind speed (U_{10} = 31.2 m/s) and drag coefficient (C_D = 0.0026) in Table 2, the parameter A equals 4.7×10^{-4}, indicating that the role of shear forces can be assumed to be negligible.

As for the mechanisms related to the wave setup/set-down, panel (a) of Figure 5 shows that the variations of $\overline{\eta}$ for non-breaking waves correlate reasonably well with the profile variance ratio, $\sigma^2_{WIND}/\sigma^2_{NO\text{-}WIND}$. The latter represents the change in wave energy caused by the wind and is hence proportional to the variation of the radiation stress.

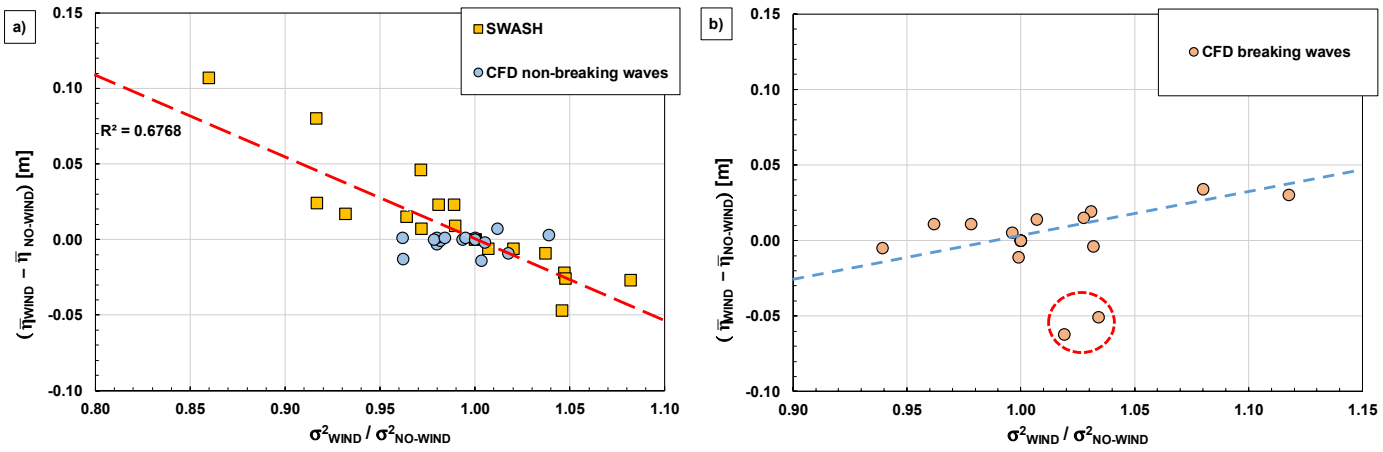

Figure 5. Variation of $\overline{\eta}$ as a function of $\sigma^2_{WIND}/\sigma^2_{NO\text{-}WIND}$ ratio. Panel (**a**): results for non-breaking waves; panel (**b**): results for breaking waves.

$\sigma^2_{WIND}/\sigma^2_{NO\text{-}WIND} < 1$ implies a reduction in dS_{xx}/dx, which, being seawards, leads the mean water level to increase (less set-down).

Since the radiation stress gradient reverses for breaking waves, the relationship between $\overline{\eta}$ and $\sigma^2_{WIND}/\sigma^2_{NO\text{-}WIND}$ also changes in sign (Figure 5b); this is except for two outliers circled in the figure, for which $\overline{\eta}$ reduces due to a reforming/rebreaking process that occurs in the innermost part of the foreshore (not shown here for brevity's sake).

However, complex the previous analysis might seem, though, it can be concluded that the observed variations of $\overline{\eta}$ are too small to have a significant effect on the mean overtopping discharge. The maximum variation recorded is nearly 0.10 m, corresponding to 4.5% of the minimum crest freeboard R_c = 2.23 m. More discussion on this point is given in Section 5.6.

5.3. Wind Stress, Wave Profiles and Overtopping Rates

It is worth noting that the results discussed in the present section were produced with the CFD numerical model only. As will be shown later, SWASH does not allow a proper assessment of the wind effects from wave profile characteristics.

For non-breaking waves Figure 6 shows that the wind shear stress produces a greater height in the up-rushing jet and pushes behind the wall the water that would otherwise have fallen back into the sea (panel (b) vs. panel (a). Such behavior is consistent with the wind effects observed by [7].

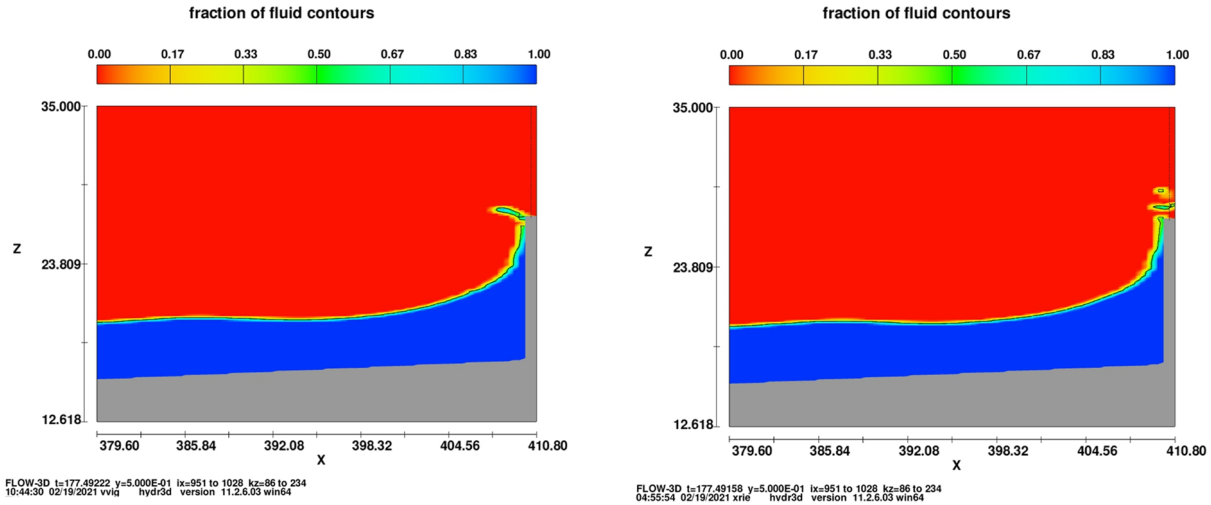

(**a**) (**b**)

Figure 6. Up-rushing jet on wave overtopping for different simulation at the time 177.5 s, TEST_3 and Rc = +8.50 m. Panel (**a**) no wind; panel (**b**) wind velocity U_{10} = 19 m/s.

Therefore, the presence of wind can cause an overtopping event that would not otherwise have occurred (Figure 7a). The consequent increase in overtopping rate due to the wind is clearly detected by comparing the cumulative overtopping volumes (Figure 7b).

On the other hand, the scenario may be different with breaking waves. As shown in Figure 8, in some cases the presence of wind may reduce the overtopping rate. As found by [52], the wind brings forward the rupture of waves because the wind pressure pushes the wave crest. This causes a reduction in the momentum of the up-rushing jet at wall, which eventually results in a lower amount of wave overtopping.

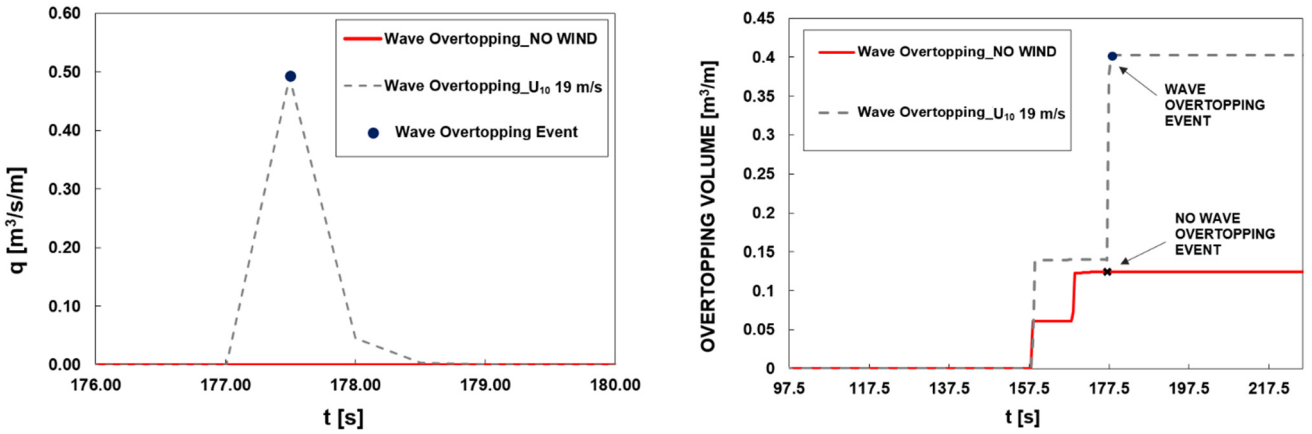

(**a**) (**b**)

Figure 7. Effects of wind stress on wave overtopping, TEST_3 and Rc +8.50 m. Panel (**a**) wind effects on overtopping discharge; panel (**b**) wind effects on cumulative wave overtopping volume.

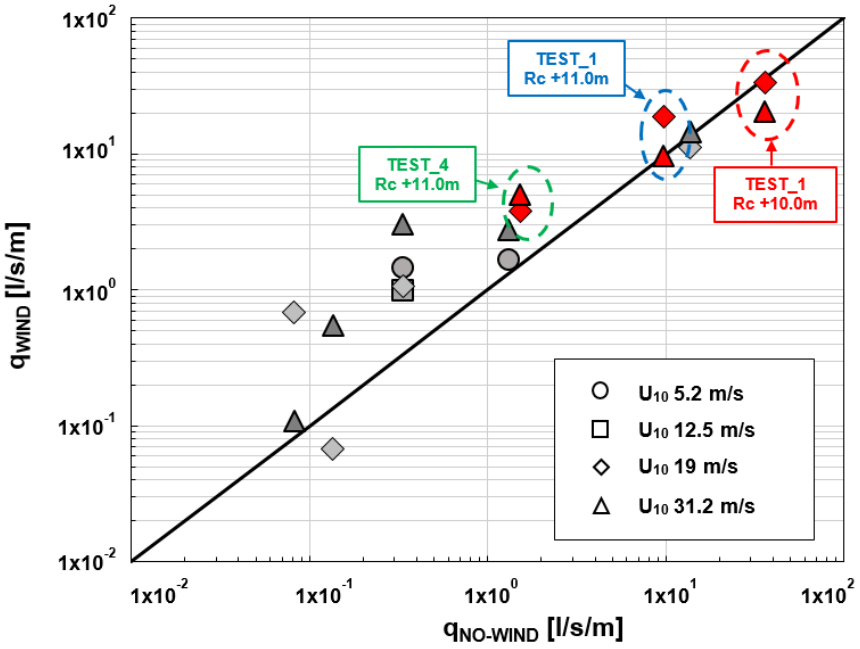

Figure 8. CFD numerical results marked with different wind speeds; red data represent breaking waves, while grey data represent non-breaking waves.

The analysis of TEST_1 (red circle in Figure 8) points out that the wind stress moves the breaking point seaward. As clearly depicted in Figure 9, the wave reaches early and seaward with the incipient breaking condition in the presence of the wind, with a much greater x-velocity at the crest. This increases the energy dissipation during the breaker movement and thus reduces the overtopping volume (Figure 10). Despite the general reduction of the overtopping rate, Figure 10 shows that the number of overtopping events increases. This behavior may be a consequence of a different energy distribution during the wave breaking process and a different redistribution of the rising flow near the wall. According to [53], the early stage of the breaking in the no wind condition is characterized by an apparently larger dissipation of energy, which leads to fewer overtopping events but with greater intensity, i.e., greater overtopping discharge.

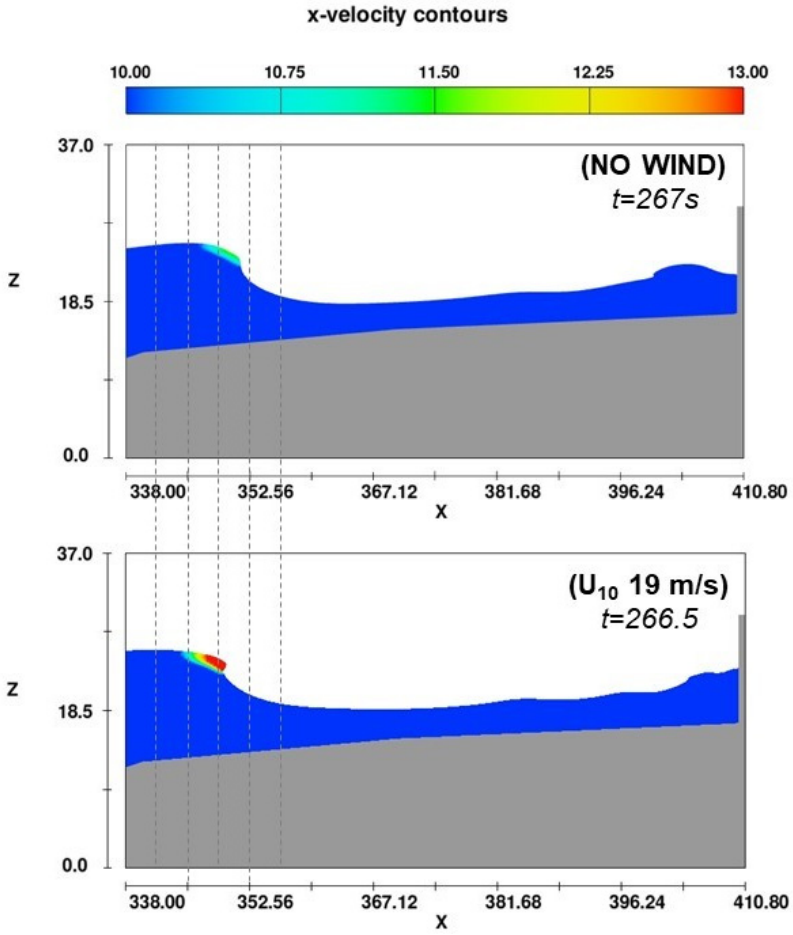

Figure 9. Incipient breaking condition with and without wind (TEST_1and Rc = +10.00 m).

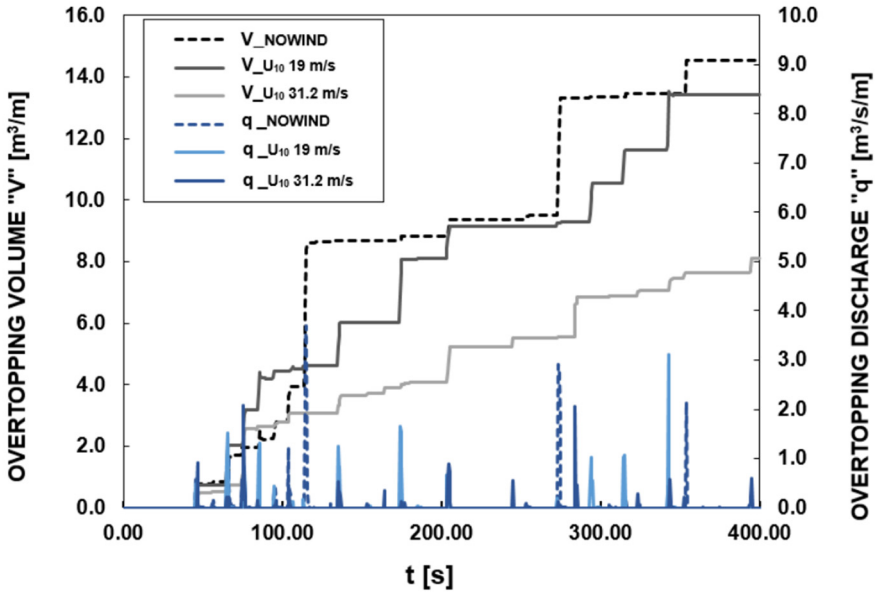

Figure 10. Cumulative overtopping volumes and wave overtopping discharges for different wind velocity, TEST_1 and Rc = +10.00 m.

However, this is not a systematic behavior. The analysis of TEST_4 (green circle in Figure 8) shows a growth of the overtopping rate in presence of wind. The difference

between these two opposing results may be probably due to the different location of the breaking point.

In Figure 11, the incipient breaking is plotted for TEST_1 and TEST_4 (blue and green circles respectively in Figure 8) under the same wind velocity and crest freeboard (Rc = +11.00 m). Since the wave of TEST_1 is steeper, the breaking point is seaward compared to TEST_4. Therefore, it could be characterized by a greater dissipation of energy, which probably leads to a reduction of the wave overtopping.

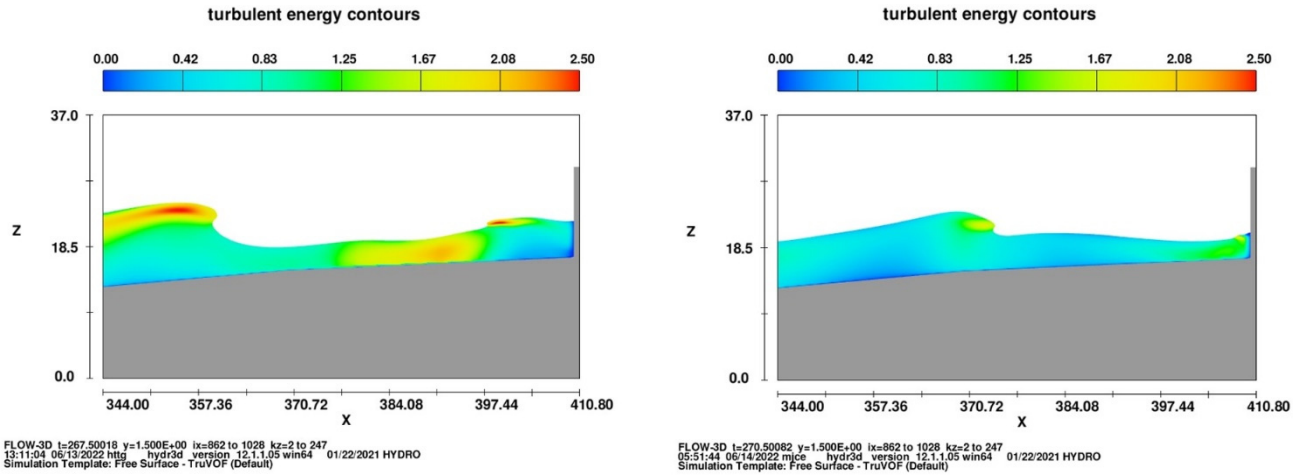

(**a**) (**b**)

Figure 11. Breaking waves under wind speed 31 m/s. Panel (**a**) TEST_1 and Rc = +11.00 m; panel (**b**) TEST_4 and Rc = +11.00 m.

Nevertheless, it is worth noting that TEST_1 and TEST_4 have different orders of magnitude of wave overtopping. This difference may have a greater impact on the final effect of the wind than the breaking process. In the Section 5.5, it will be demonstrated that the influence of the wind mostly depends on the magnitude of the overtopping discharge.

Finally, we have observed that a higher wind velocity does not always produce a greater increase in the overtopping rate. This is consistent with [20], who have found that the overtopping rate does not increase monotonically with wind velocity, but that there is an effective range of relative wind speed which significantly affects the overtopping rate.

5.4. Numerical Experiments vs. Pullen et al.'s Physical Model Data

In Figure 11, numerical results carried out with FLOW-3D and SWASH are compared with the experimental data reported in [5].

The range of wind speeds investigated in this study is quite similar to that of [5] (i.e., 15, 26 and 28 m/s).

As reported in [5] and also observed by [3,25], FLOW-3D and SWASH confirm that the wind has no effect on the "green water" overtopping regime ($q_{NO\text{-}WIND}$ greater than 100 l/s/m).

On the other hand, the influence of the wind increases when the flow rate decreases. The CFD model reproduces this behavior well; its data spread within the same cloud as those of [4], though the numerical outcomes appear to be somewhat more scattered (Figure 12). Physical and CFD results are therefore in good agreement, even though [5] only examined the wind effect in front of the seawall (i.e., only the convective transport over the wall).

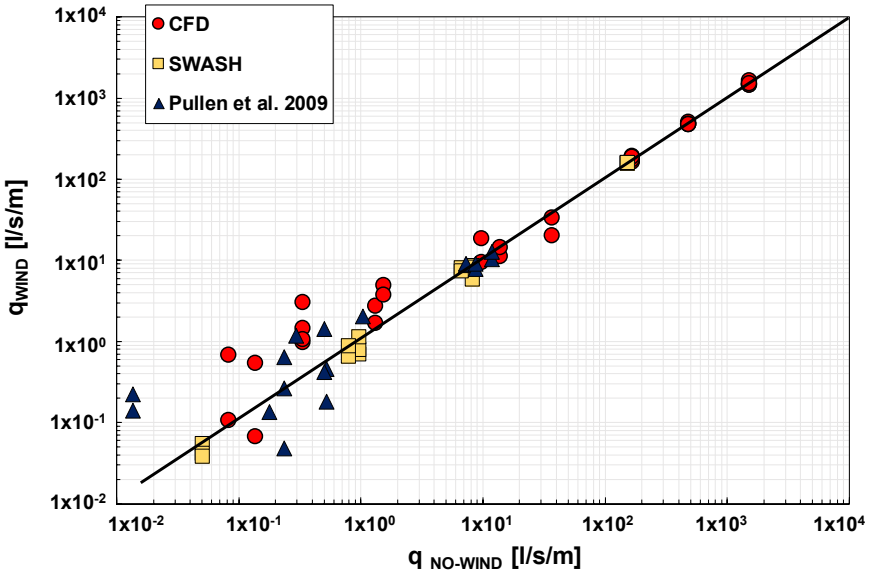

Figure 12. Numerical results vs HRW laboratory experiments of mean overtopping discharges [5] with and without wind.

Conversely, SWASH appeared unable to reproduce the wind effect on the lower overtopping discharges. Analyzing different orders of magnitude of q, the effect of wind was always negligible. An increase in discharge was not observed (Figure 12). The slight variations in q_{WIND} indicated that the results were affected by the wind stress term, but not appropriately. SWASH appears unsuitable to reproduce the phenomenon dealt with in this study. This is probably due to the structure of SWASH, which is a depth-integrated model that cannot simulate the water separation phase in front of the wall. Therefore, it does not reproduce the increase in the overtopping rate due to the wind typical of the lower overtopping regime, where the spray blown over the wall is the predominant mechanism. This is clearly shown in the next section.

5.5. The Wind Factor f_{WIND}

The effect of the wind on the mean overtopping discharge is quantitatively expressed by the wind factor f_{WIND}, i.e., the mean overtopping discharge with wind and that without wind ratio.

The results of the CFD tests (Figure 13) showed that f_{WIND} is equal to 1 when the discharge is greater than 10^2 l/s/m; then, a transition zone is discernible, where the wind has an unsystematic effect and can even reduce the overtopping discharge (between 10^1 and 10^2 l/s/m); and finally, in a zone with a lower overtopping regime, the data clearly demonstrated an increase in the overtopping rate due to the wind ($f_{WIND} > 1$).

The wind factor appears to be significantly affected by the magnitude of wave overtopping.

In order to understand how the influence of wind changes by reducing the amount of wave overtopping, three different orders (circled in red in Figure 13) were analyzed, namely 10^2 l/s/m, 10^0 l/s/m and 10^{-1} l/s/m.

For green water ($q_{NO\text{-}WIND} > 100$ l/s/m), there were no significant differences in the horizontal velocity and thickness of the overtopping layer when comparing wind and no wind conditions (Figure 14). The wind effect seems to be negligible as compared to the momentum of overtopping water, so that the mean overtopping discharge is not influenced by the wind. Thus, f_{WIND} is almost 1.

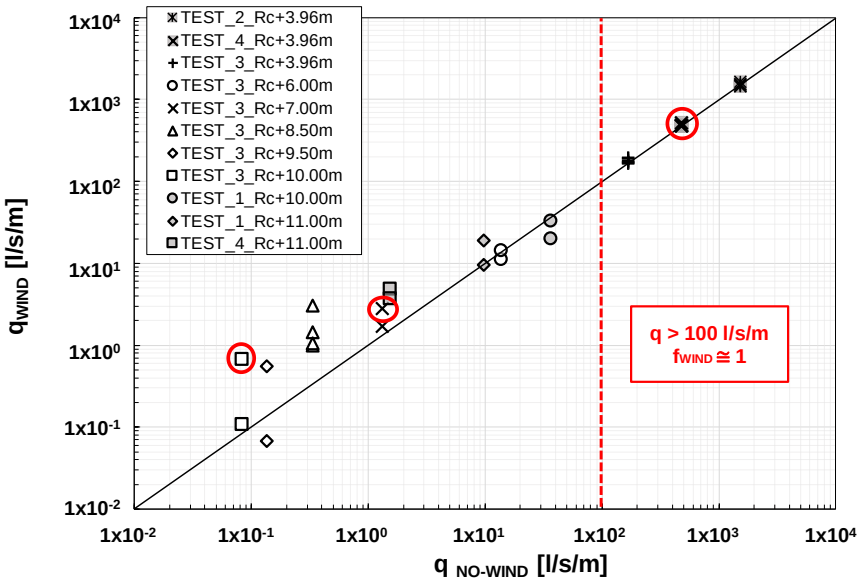

Figure 13. Numerical results of wind influence with different wave conditions and different Rc.

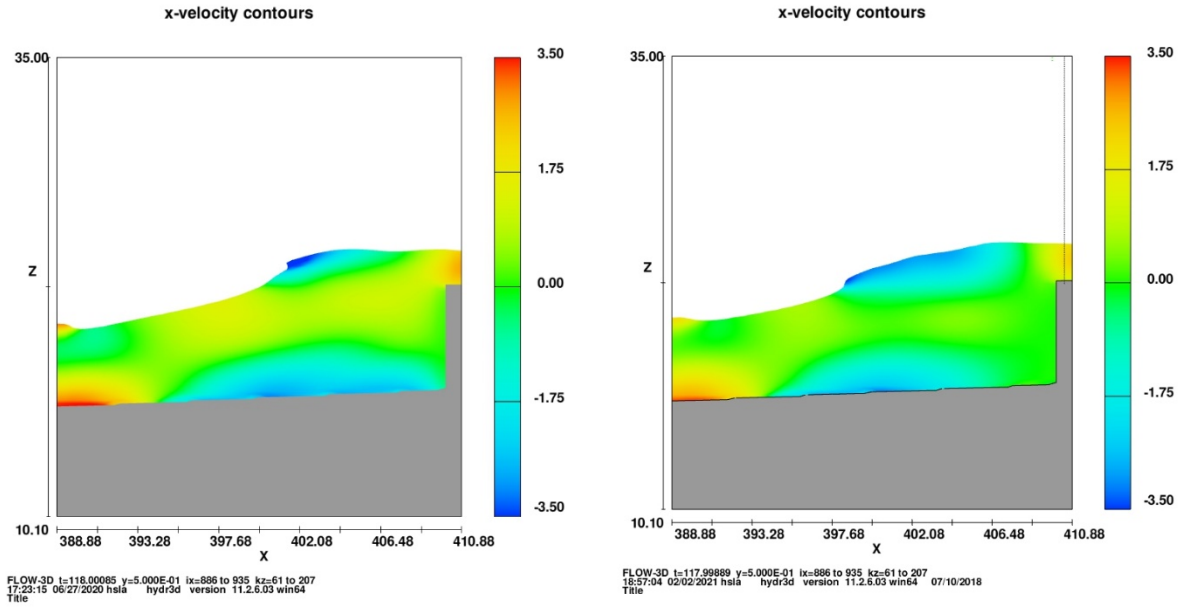

(**a**) (**b**)

Figure 14. TEST_2 and Rc = +3.96 m. Panel (**a**) no wind; panel (**b**) U_{10} 30 m/s.

On the other hand, for a mean overtopping discharge of the order of 10^0 l/s/m, the comparison in Figure 15 shows that the wind effect cannot be neglected. The wind stress lead to a greater height of the up-rushing jet, the difference of height being about 0.3 m (the water spray was not considered). Moreover, unlike the no wind condition, the fluid stream and the water spray were characterized by a landward velocity (Figure 15b), which ensured that the water crossed the wall instead of falling back into the numerical flume (Figure 15a). Therefore, the presence of wind increased the overtopping rate by inducing a greater height of the up-rushing jet and by transporting water spray over the seawall. The overtopping rates of the order of 10^0 l/s/m are thus characterized by a wind factor f_{WIND} greater than 1.

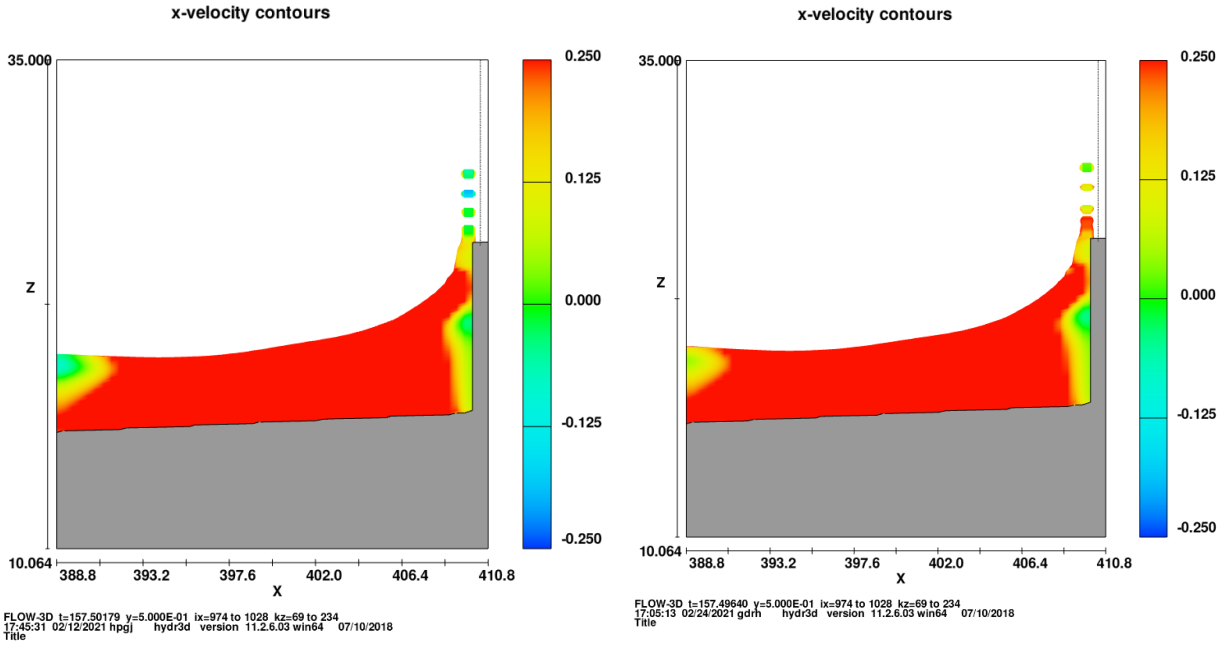

(**a**) (**b**)

Figure 15. TEST_3 and Rc = +7.00 m. Panel (**a**) no wind; panel (**b**) U_{10} 31.2 m/s.

Reducing the discharge to 10^{-1} l/s/m, the main mechanism was the advection of the spray by the wind, i.e., "white water" overtopping. In fact, as shown in Figure 16, the overtopping occurred when the spray crossed the seawall. The water spray may be carried over the wall under its own momentum without wind, otherwise it falls back into the sea (Figure 16a). Onshore wind, on the other hand, significantly increased the amount of spray that crossed the wall (Figure 16b) and thus played a key role in the overtopping process. The difference between wind and no wind conditions was remarkable. Therefore, the wind factor reached its maximum value, as reported in Figure 17.

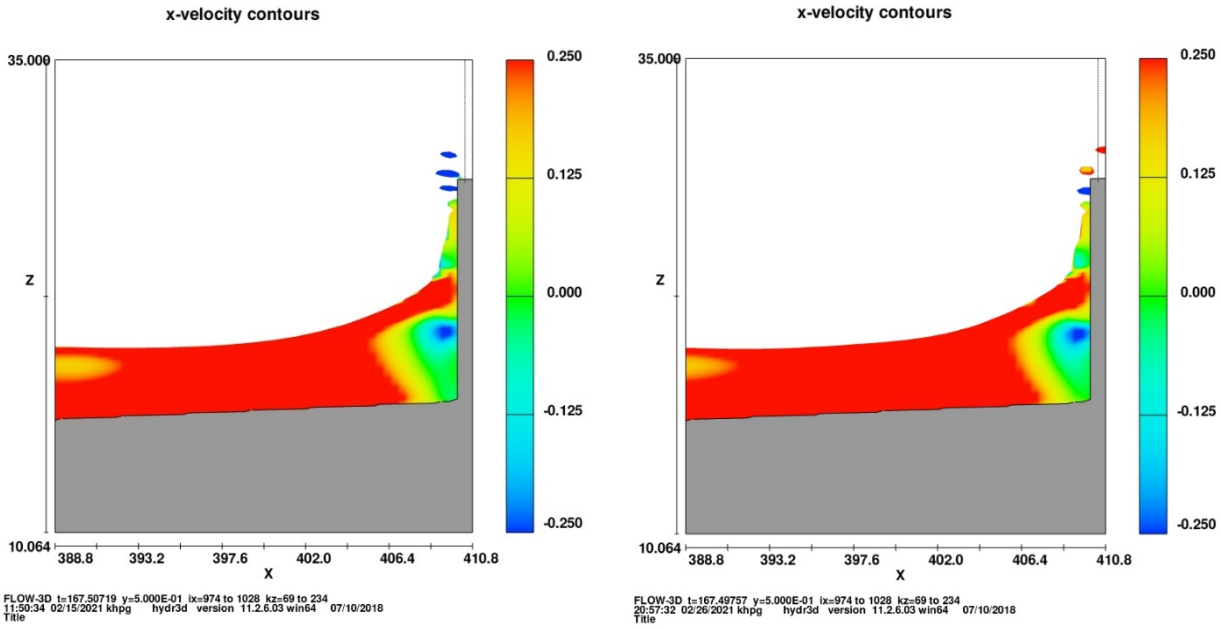

(**a**) (**b**)

Figure 16. TEST_3 and Rc = +10.00 m. Panel (**a**) no wind; panel (**b**) U_{10} 19 m/s.

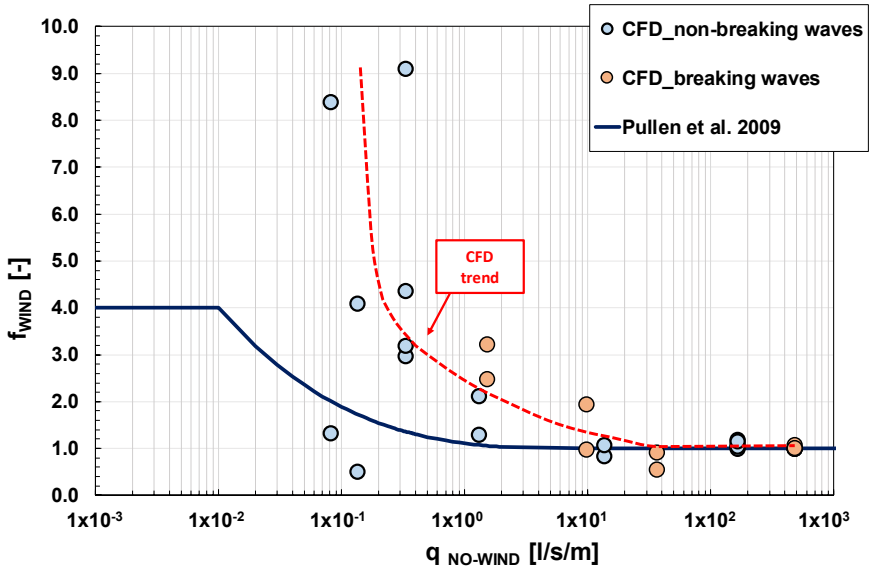

Figure 17. Comparison between numerical and physical f_{WIND} trends [5].

5.6. Quantitative Analysis

In Figure 17, the CFD wind factor was plotted in the function of the mean overtopping dis-charge, $q_{NO\text{-}WIND}$. Equation (1) was drawn as well.

The numerical wind factors follow a decreasing trend for $10^{-1} < q_{NO\text{-}WIND} < 10^{1}$ l/s/m, while they remain close to unity at higher rates.

Breaking and non-breaking waves appear to behave similarly, even if some breaking data lie above the non-breaking points.

The observed scatter is not surprising, since the wind factor is essentially controlled by the number of droplets produced during the up-rush phase, which is a highly random process. Since the incoming wave trains are identical with and without the wind (both in the frequency and time domains), the inherent uncertainty related to the overtopping phenomenon has likely a negligible impact on the observed results [54].

Most interestingly, however: present experiments exhibit larger values of f_{WIND} compared to Equation (1); the wind factor increases rather fast and reaches a value in the order of 10 for $q_{NO\text{-}WIND} = 10^{-1}$ l/s/m, while Equation (1) predicts 2. On the other hand, the overtopping process is unaffected by the presence of wind from $q_{NO\text{-}WIND}$ = O (10^2), rather than O (10^1).

It is worth highlighting that the observed behavior is practically independent of the variations in the mean water level discussed in Section 5.2. This is shown in Figure 18, where the largest values of the wind factor are attained with no difference between $\overline{\eta_{WIND}}$ and $\overline{\eta_{NO-WIND}}$. Conversely, the opposite is found with growing the variation in the mean water level (e.g., -0.06 R_c), $f_{WIND} = 1$.

The previously discussed results were compared with physical model experiments conducted at Plymouth University by Durbridge [27]. The author performed random and periodic 2D-tests, at scale of 1:21, on a shallow foreshore vertical seawall. Unlike this study, Durbridge's tests focused on the effect of wave frequency, while the structure's freeboard was left constant along with the offshore wave height.

Analogous to what was discussed above, the author found values of f_{WIND} that largely exceeded Equation (1), being significantly larger than unity also for values of $q_{NO\text{-}WIND}$ of the order of 10 l/s/m. Like in Figure 17, the maximum measured enhancement factor is of the order of 10.

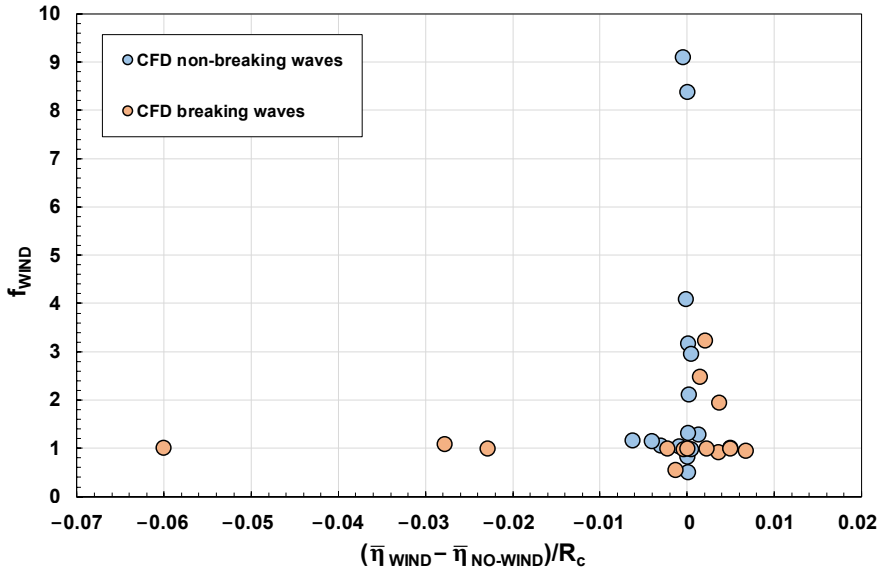

Figure 18. CFD wind factors in function of the ratio between the variation in $\overline{\eta}$ due to the wind and the crest freeboard.

This indicates the need for new predictive equations, which include more variables than the sole mean overtopping discharge.

Figure 19 plots CFD and Durbridge' data against the shallow water sea-age coefficient:

$$S_{s-a} = \frac{U}{\sqrt{g\left(h_{TOE} + H_{deep}\right)}} \tag{19}$$

where H_{deep} equals offshore H_{m0} in the case of random waves.

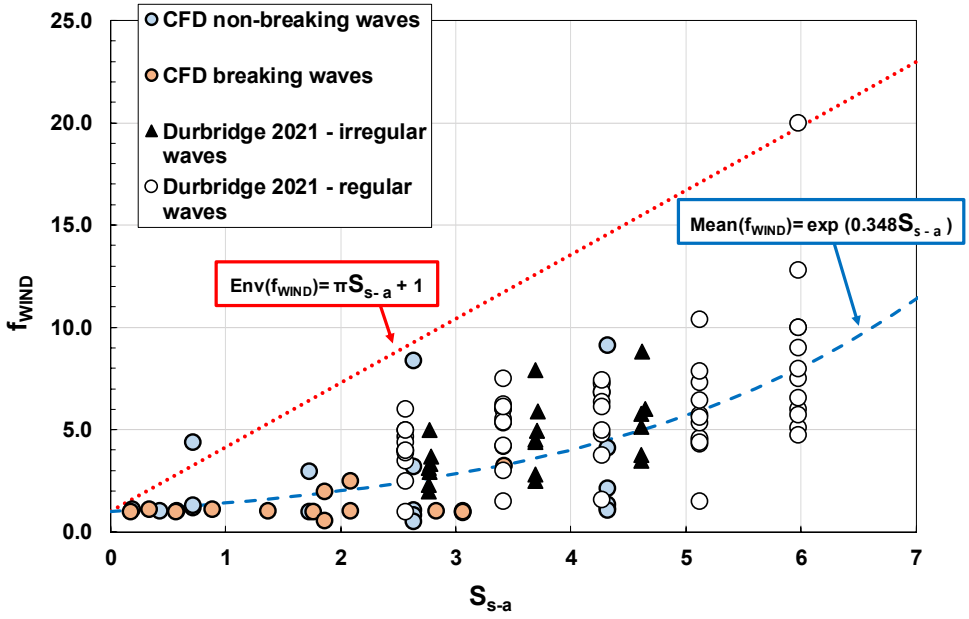

Figure 19. Comparison between numerical and literature [27] results.

Numerical and physical data appear reasonably consistent with each other, in spite of the inherent scatter that affects the process under study. Consistent to [21], the enhancement factor increases with the wind speed, and exceeds 1 for sea-age coefficients larger than 2.

Based on these results, two tentative formulae are suggested, which represent, respectively, the mean trend and the envelope of data. The equations are:

$$Env\ (f_{wind}) = 1 + \pi \cdot S_{s-a} \tag{20}$$

$$Mean\ (f_{wind}) = \exp(0.348 \cdot S_{s-a}) \tag{21}$$

6. Discussion and Conclusions

The main purposes of this work were to verify the ability of simplified numerical models to capture the macroprocesses involved in the phenomenon of wave overtopping in the presence of onshore wind.

In this view, a single fluid RANS model and the SWASH model, based on the Non-Linear Shallow Water Equations, were employed to investigate the response of a vertical seawall. Numerical outcomes were compared with the literature, either with reference to predictive equations or physical model data.

The roughest simplification of our modeling consists in using a single fluid, with the effect of wind being simulated via an appropriate shear stress, calculated with one of the most recent and accurate formulations for wind drag (Equation (15)). Obviously, since the drag coefficient varies with wind speed, the effects of the Reynolds number are theoretically accounted for.

As general result, we demonstrated that the application of wind stress induces negligible variations in the mean water level, which was predictable as our numerical flume measures only 410 m in length. Hence, the process under study is essentially governed by the effects the wind shear exerts on the wave profile. These include:

- Deformation of the run-up wedge;
- Advection of the droplets formed in the uprush phase;
- Variation in the breaking point with wind.

The CFD RANSE model was found to address all the above processes realistically. According to [7,25], the numerical experiments have shown that the wind stress gives rise to higher up rushing jets, and pushes forward the water spray that would otherwise have fallen back into the sea (Figure 5). This can be considered one of the leading mechanisms for the increase of the overtopping rate by wind.

Our tests also suggest that the effect of wave breaking should be considered with some caution. On the one side, breaking waves may lead to larger wind enhancement factors by augmenting the number of droplets available for advection; however, as the wind moves the breaking point seawards, there might be a reduction in the overtopping volume as a consequence of the larger dissipation of energy.

In Figure 17, the effect of wind is seen to increase with reducing the overtopping regime; this result is in qualitative agreement with [5], and can be explained by the fact that the influence of the droplets' advection on the mean overtopping rate increases with reducing q. However, the results of CFD experiments differ from Pullen et al.'s in two essential points, namely:

- the wind enhancement factor reaches the value of 10 rather than a maximum of 4;
- The effect of wind keeps on resenting for overtopping regimes as intense as 100 l/s/m, rather than vanishing at 1 l/s/m.

Further analyses revealed that those numerical results are consistent with a recent laboratory study conducted by [27] at the University of Plymouth (UK). By gathering Durbridge data and CFD tests, two new predictive equations have been developed, which return the wind enhancement factor in the function of wind speed, local water depth and offshore wave height (Equations (21) and (22)).

Numerical results carried out via SWASH shows that it is probably not suitable for reproducing the influence of the wind. Even with mean overtopping discharge lower than 1 l/s/m, the wind does not increase the overtopping rate. This is probably due to the structure of SWASH, which is a depth-integrated model that cannot simulate the water

separation phase in front of the wall. Therefore, it does not reproduce the increase in the overtopping rate due to the wind typical of the lower overtopping regime, where the spray blown over the wall is the predominant enhancement mechanism.

As a last remark, it is worth commenting that all the data presented in this study feature a remarkable scatter. Since numerical experiments are carried out, by nature, under the most controlled conditions, this scatter must be attributed to the inherent randomness of the wind enhancement process, rather than to the wave overtopping phenomenon. The scatter in wave overtopping observed in the literature is mostly due to laboratory effects, measurement issues (at low rates) and time-domain differences among the wave series, as shown in [54]. None of the previous cases applies to the present numerical experiments. We also note that while overtopping scatter can be either positive or negative, with a zero mean, the effects discussed in this paper lead almost invariably to an increase of the mean discharge.

All in all, the same conclusion holds for Pullen et al. and Durbridge's experiments.

In conclusion, the effect of wind influence on wave overtopping was successfully studied using CFD and the results are in agreement with the literature, although a single-fluid approach was adopted. Furthermore, two new predictive equations for the wind transport factor were developed.

Future research will focus on a two-fluids approach to deepen analyze the effects of wind on wave overtopping. Therefore, the impact of the adopted approach on the results will be verified by comparing a more sophisticated and a simplified wind modelling.

Author Contributions: Conceptualization, A.D.L., S.T. and M.B.; methodology, F.D., M.B. and E.P.C.; software, F.D., A.D.L. and S.T.; validation. M.B. and F.D.; investigation, A.D.L. and S.T.; data curation, A.D.L., S.T. and M.B.; writing—original draft preparation, A.D.L. and S.T.; writing—review and editing, A.D.L., S.T., F.D. and M.B.; supervision, E.P.C. All authors have read and agreed to the published version of the manuscript.

Funding: This research received no external funding.

Institutional Review Board Statement: Not applicable.

Informed Consent Statement: Not applicable.

Data Availability Statement: Data are available from the corresponding author upon request.

Conflicts of Interest: The authors declare no conflict of interest.

References

1. Van der Werf, I.M.; Van Gent, M.R.A. Wave Overtopping over Coastal Structures with Oblique Wind and Swell Waves. *J. Mar. Sci. Eng.* **2018**, *6*, 149. [CrossRef]
2. EurOtop. *Manual on Wave Overtopping of Sea Defences and Related Structures*; Van der Meer, J.W., Allsop, N.W.H., Bruce, T., De Rouck, J., Kortenhaus, A., Pullen, T., Schüttrumpf, H., Troch, P., Zanuttigh, B., Eds.; 2018. Available online: www.overtopping-manual.com (accessed on 10 December 2018).
3. de Waal, J.P.; Tönjes, P.; van der Meer, J. Wave overtopping of vertical structures including wind effect. In Proceedings of the 25th International Conference on Coastal Engineering, ASCE, Orlando, FL, USA, 2–6 September 1996. [CrossRef]
4. De Rouck, J.; Geeraerts, J.; Troch, P.; Kortenhaus, A.; Pullen, T.; Franco, L. New results on scale effects for wave overtopping at coastal structures. In Proceedings of the International Conference on Coastlines, Structures and Breakwaters, London, UK, 19–21 April 2005.
5. Pullen, T.; Allsop, W.; Bruce, T.; Pearson, J. Field and laboratory measurements of mean overtopping discharges and spatial distributions at vertical seawalls. *Coast. Eng.* **2009**, *56*, 121–140. [CrossRef]
6. Murakami, K.; Maki, D.; Ogino, K. Effect of Wind Velocity on Wave Overtopping. In Proceedings of the 10th International Conference on Asian and Pacific Coasts (APAC 2019), Hanoi, Vietnam, 25–28 September 2019.
7. Kiku, M.; Kawasaki, K. Proposal of numerical wave flume for wave overtopping computation considering wind external force. In Proceedings of the 34th Conference on Coastal Engineering, Seoul, Republic of Korea, 15–20 June 2014.
8. De Chowdhury, S.; Causon, D.; Qian, L.; Mingham, C.; Chen, H.; Lin, Z.; Zhou, J.G.; Pullen, T.; Silva, E.; Hu, K.; et al. Investigation of Wind Effects on Wave Overtopping at Sea Defences. In Proceedings of the Coastal Structures 2019, Hannover, Germany, 29 September–2 October 2019; Bundesanstalt für Wasserbau. S: Karlsruhe, Germany, 2019; pp. 841–850. [CrossRef]
9. Xie, Z. Numerical modelling of wind effects on breaking solitary waves. *Eur. J. Mech. B-Fluid* **2014**, *43*, 135–147. [CrossRef]

10. Malara, G.; Kougioumtzoglou, I.A.; Arena, F. Extrapolation of random wave field data via compressive sampling. *Ocean Eng.* **2018**, *157*, 87–95. [CrossRef]
11. Bayındır, C.; Namlı, B. Efficient sensing of the von Karman vortices using compressive sensing. *Comput. Fluids* **2021**, *226*, 104975. [CrossRef]
12. Alan, A.R.; Bayindir, C. Analysis of Wave Runup, Overtopping and Overwash Parameters via Compressive Sensing. In Proceedings of the International Conference on Applied Mathematics in Engineering (ICAME), Balikesir, Turkey, 1–3 September 2021.
13. Flow Science, Inc. *FLOW-3D User's Manual*, HYDRO ed.; Flow Science, Inc.: Santa Fe, NM, USA, 2022.
14. Zijlema, M.; Stelling, G.; Smit, P. SWASH: An operational public domain code for simulating wave fields and rapidly varied flows in coastal waters. *Coast. Eng.* **2011**, *58*, 992–1012. [CrossRef]
15. Vicinanza, D.; Dentale, F.; Salerno, D.; Buccino, M. Structural response of seawave slot-cone generator (SSG) from random wave CFD simulations. In Proceedings of the Twenty-fifth International Ocean and Polar Engineering Conference, Kona, HI, USA, 21–26 June 2015.
16. Di Leo, A.; Reale, F.; Dentale, F.; Viccione, G.; Carratelli, E.P. Wave-structure interactions a 2d innovative numerical methodology. In Proceedings of the 23rd Conference of the Italian Association of Theoretical and Applied Mechanics, Salerno, Italy, 4–7 September 2017; Volume 2, pp. 1699–1708.
17. Dentale, F.; Reale, F.; Di Leo, A.; Pugliese Carratelli, E. A CFD approach to rubble mound breakwater design. *Int. J. Nav. Archit. Ocean. Eng.* **2018**, *10*, 644–650. [CrossRef]
18. Buccino, M.; Daliri, M.; Dentale, F.; Di Leo, A.; Calabrese, M. CFD experiments on a low crested sloping top caisson breakwater. Part 1. nature of loadings and global stability. *Ocean Eng.* **2019**, *182*, 259–282. [CrossRef]
19. Buccino, M.; Daliri, M.; Dentale, F.; Calabrese, M. CFD experiments on a low crested sloping top caisson breakwater. Part 2. Analysis of plume impact. *Ocean Eng.* **2019**, *173*, 345–357. [CrossRef]
20. Di Leo, A. CFD Analysis of Coastal Flood Risk: Overtopping Related Phenomena. Ph.D. Thesis, University of Salerno, Department of Civil Engineering, Fisciano, Italy, 2021.
21. Hieu, P.D.; Vinh, P.N.; Toan, D.V.; Son, N.T. Study of Wave-wind Interaction at a Seawall Using a Numerical Wave Channel. *Appl. Math. Model.* **2014**, *38*, 5149–5159. [CrossRef]
22. Di Leo, A.; Buccino, M.; Dentale, F.; Pugliese Carratelli, E. CFD Analysis of Wind Effect on Wave Overtopping. In Proceedings of the 32nd International Ocean and Polar Engineering Conference, Shanghai, China, 5–10 June 2022.
23. Zhang, N.; Zhang, Q.; Wang, K.H.; Zou, G.; Jiang, X.; Yang, A.; Li, Y. Numerical simulation of wave overtopping on breakwater with an armor layer of accropode using SWASH model. *Water* **2020**, *12*, 386. [CrossRef]
24. Suzuki, T.; Altomare, C.; Veale, W.; Verwaest, T.; Trouw, K.; Troch, P.; Zijlema, M. Efficient and robust wave overtopping estimation for impermeable coastal structures in shallow foreshores using SWASH. *Coast. Eng.* **2017**, *122*, 108–123. [CrossRef]
25. Ward, D.L.; Zhang, J.; Wibner, C.G.; Cinotto, C.M. Wind effects on runup and overtopping. In Proceedings of the 25th International Conference on Coastal Engineering (ICCE 1996), Orlando, FL, USA, 2–6 September 1996; ASCE: New York, NY, USA, 1996; pp. 2206–2215.
26. Wolters, G.; van Gent, M.R.A. Maximum wind effect on wave overtopping of sloped coastal structures with crest elements. In Proceedings of the 5th International Coastal Structures, Venice, Italy, 2–4 July 2007; pp. 1263–1274.
27. Durbridge, S. The effect of onshore wind on wave overtopping of a vertical sea wall. *Plymouth Stud. Sci.* **2021**, *14*, 311–355.
28. Bradford, S.F. Numerical simulation of surf-zone dynamics. *J. Waterw. Port Coast. Ocean Eng.* **2000**, *126*, 1–13. [CrossRef]
29. Hirt, C.W.; Nichols, B.D. Volume of fluid (VOF) method for the dynamics of free boundaries. *J. Comput. Phys.* **1981**, *39*, 201–225. [CrossRef]
30. Hirt, C.W.; Sicilian, J.M. A porosity technique for the definition of obstacles in rectangular cell meshes. In Proceedings of the Fourth International Conference of Ship Hydrodynamics, National Academy of Science, Washington, DC, USA, 24–27 September 1985.
31. Smit, P.; Zijlema, M.; Stelling, G. Depth-induced wave breaking in a non-hydrostatic, near-shore wave model. *Coast. Eng.* **2013**, *76*, 761–816. [CrossRef]
32. Delft University of Technology. *SWASH User's Manual, Version 8.01*; GA: Delft, The Netherlands, 2021–2022.
33. Chen, Q.; Kaihatu, J.M.; Hwang, P.A. Incorporation of wind effects into Boussinesq wave models. *J. Waterw. Port Coast. Ocean Eng.* **2004**, *130*, 312–321. [CrossRef]
34. Lopez, L.F.C.; Salerno, D.; Dentale, F.; Capobianco, A.; Buccino, M. Experimental campaign on the overtopping of the seawall Malecon Traditional. In Proceedings of the 25th International Ocean and Polar Engineering Conference (ISOPE), Kona, HI, USA, 21–26 June 2015.
35. Bretschneider, C.L. *Generation of Waves by Wind: State of Art*; International Summer Course: Lunteren, The Netherlands, 1–18 September 1964.
36. Andreas, E.L.; Mahrt, L.; Vickers, D. A New Drag Relation for Aerodynamically Rough Flow over the Ocean. *J. Atmos. Sci.* **2012**, *69*, 2520–2537. [CrossRef]
37. Wu, J. Wind-stress coefficients over sea surface from breeze to hurricane. *J. Geophys. Res.* **1982**, *87*, 9704–9706. [CrossRef]
38. Buccino, M.; Daliri, M.; Calabrese, M.; Somma, R. A numerical study of arsenic contamination at the Bagnoli bay seabed by a semi-anthropogenic source. Analysis of current regime. *Sci. Total Environ.* **2021**, *782*, 146811. [CrossRef]

39. Buccino, M.; Daliri, M.; Buttarazzi, M.N.; Del Giudice, G.; Calabrese, M.; Somma, R. Arsenic contamination at the Bagnoli Bay seabed (South Italy) via particle tracking numerical modeling: Pollution patterns from stationary climatic forcings. *Chemosphere* **2022**, *303*, 134955. [CrossRef]
40. Fenton, J.D. Numerical Methods for Nonlinear Waves. In *Advances in Coastal and Ocean Engineering*; Liu, P.L.-F., Ed.; World Scientific: Singapore, 1999; Volume 5, pp. 241–324.
41. USACE (U.S. Army Corps of Engineers). *Coastal Engineering Manual, EM 1110-2-1100*; USACE: Washington, DC, USA, 2006.
42. Symonds, G.; Huntley, D.A.; Bowen, A.J. Two-dimensional surf beat: Long wave generation by a time-varying breakpoint. *J. Geophys. Res. Oceans* **1982**, *87*, 492–498. [CrossRef]
43. Durbin, P.A. On the k-3 stagnation point anomaly. *Int. J. Heat Fluid Flow* **1996**, *17*, 89–90. [CrossRef]
44. Larsen, B.E.; Fuhrman, D.R. On the over-production of turbulence beneath surface waves in Reynolds-averaged Navier-Stokes models. *J. Fluid Mech.* **2018**, *853*, 419–460. [CrossRef]
45. Zelt, J.A.; Skjelbreia, J.E. Estimating incident and reflected wave fields using an arbitrary number of wave gauges. In Proceedings of the 23rd International Conference on Coastal Engineering (ICCE), Venice, Italy, 4–9 October 1992; ASCE: Reston, VA, USA, 1992; Volume 1, pp. 777–789. [CrossRef]
46. Resio, D.T. Assesment of Wind Effects on Wave Overtopping of Proposed Virginia Beach Seawall. Technical Memorandum to CERC, OCTI. 1987.
47. Dean, R.G.; Dalrymple, R.A. *Coastal Processes with Engineering Applications*; Cambridge University Press: New York, NY, USA, 2001.
48. Longuet-Higgins, M.S.; Stewart, R.W. Radiation stress and mass transport in gravity waves, with application to 'surf beats'. *J. Fluid Mech.* **1962**, *13*, 481–504. [CrossRef]
49. Galvin, C.J., Jr. Breaker type classification on three laboratory beaches. *J. Geophys. Res.* **1968**, *73*, 3651–3659. [CrossRef]
50. Basco, D.R. A qualitative description of wave breaking. *J. Waterw. Port Coast. Ocean Eng.* **1985**, *111*, 171–188. [CrossRef]
51. Calabrese, M.; Buccino, M.; Pasanisi, F. Wave breaking macrofeatures on a submerged rubble mound breakwater. *J. Hydro-Environ. Res.* **2008**, *1*, 216–225. [CrossRef]
52. Nagai, S.; Ueda, S. Study on the shape and structure of seawall considering wind and waves. In Proceedings of the Coastal Engineering, JSCE, The Hague, The Netherlands, 29 January 1960.
53. Perlin, M.; Wooyoung, C.; Zhigang, T. Breaking Waves in Deep and Intermediate Waters. *Annu. Rev. Fluid Mech.* **2013**, *45*, 115–145. [CrossRef]
54. Romano, A.; Bellotti, G.; Briganti, R.; Franco, L. Uncertainties in the physical modelling of the wave overtopping over a rubble mound breakwater: The role of the seeding number and of the test duration. *Coast. Eng.* **2015**, *103*, 15–21. [CrossRef]